

50nW Opamp-Less $\Delta\Sigma$ -Modulated Bioimpedance Spectrum Analyzer for Electrochemical Brain Interfacing

Maged ElAnsary[✉], Member, IEEE, Nima Soltani, Member, IEEE, Hossein Kassiri[✉], Member, IEEE, Ruben Machado, Suzie Dufour, Peter L. Carlen, Michael Thompson, Senior Member, IEEE, and Roman Genov[✉], Senior Member, IEEE

Abstract—A fully integrated 130 nm CMOS 12-channel biofouling-resistant potassium-selective brain neurochemistry impedance spectrum analyzer is presented. Each 0.004 mm² channel is an amperometric readout circuit composed of an opamp-less delta-sigma-modulated analog-to-digital converter (ADC) that consumes only 50 nW of power from a 0.6 V supply. The latter is analytically proven to be approximately equivalent to the former under conditions that are typical for the biochemical microsensors. The circuit also includes a low-power multiplierless frequency response analysis (FRA) unit that performs bioimpedance extraction. The channel achieves 1 pA current sensitivity and attains 50.3 dB signal-to-noise-and-distortion ratio (SNDR). The impedance analyzer achieves a dynamic range of 1 pA to 20 nA and a 5 kHz frequency scan range. The 2 mm × 1 mm die has been validated *in vivo* in real-time multisite potassium sensing in the rodent brain using gold microelectrodes implemented on a polyimide substrate.

Index Terms—Affinity-based sensors, amperometry, analog-to-digital converter (ADC), animal model, axon, biofouling, biosensor, calibration curve, CMOS, comparator, delta-sigma, EEG, electrochemical cell, electrochemical impedance spectroscopy (EIS), electrochemical sensors, epilepsy, frequency response analysis (FRA), integrated circuit (IC), integrator, ion channel, ionophore, loop gain, microelectrode, magnetic resonance imaging (MRI), multichannel, opamp-less, oversampling ratio, passive integrator, potassium sensing, potentiostat, voltammetry.

Manuscript received April 25, 2019; revised September 24, 2019 and January 19, 2020; accepted March 4, 2020. Date of publication March 24, 2020; date of current version June 29, 2020. This article was approved by Associate Editor Hoi-Jun Yoo. This work was supported in part by the Natural Sciences and Engineering Research Council (NSERC) of Canada and in part by the Canada Foundation for Innovation. (*Corresponding author: Maged ElAnsary*)

Maged ElAnsary, Nima Soltani, Hossein Kassiri, and Roman Genov are with the Department of Electrical and Computer Engineering, University of Toronto, Toronto, ON M5S 3G4, Canada (e-mail: maged.elansary@mail.utoronto.ca; roman@eecg.utoronto.ca).

Ruben Machado is with the Department of Chemistry, University of Toronto, Toronto, ON M5S 3H6, Canada.

Suzie Dufour is with the Toronto Western Research Institute, Fundamental Neurobiology Division, Toronto, ON M5T 2S8, Canada.

Peter L. Carlen is with the Toronto Western Research Institute, Fundamental Neurobiology Division, Toronto, ON M5T 2S8, Canada, and also with the Institute of Biomaterials and Biomedical Engineering, University of Toronto, Toronto, ON M5S 3G9, Canada.

Michael Thompson is with the Department of Chemistry, University of Toronto, Toronto, ON M5S 3H6, Canada, and also with the Institute of Biomaterials and Biomedical Engineering, University of Toronto, Toronto, ON M5S 3G9, Canada.

Color versions of one or more of the figures in this article are available online at <http://ieeexplore.ieee.org>.

Digital Object Identifier 10.1109/JSSC.2020.2981033

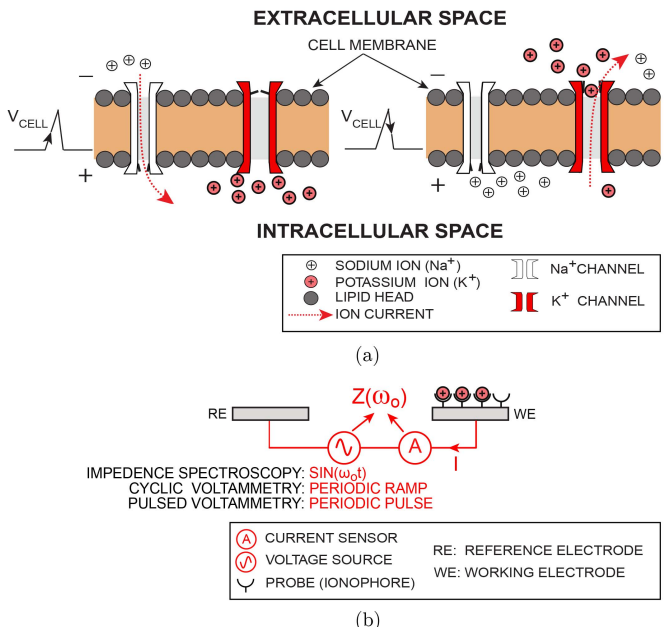


Fig. 1. Action potential creation through voltage-gated ion channels. (a) Depolarization: Na^+ channels open and Na^+ moves into the axon. Repolarization: K^+ channels open and K^+ moves out of the axon, creating a change in polarity between the outside and the inside of the cell. (b) Potassium-ion-sensitive microelectrode: electrode surface are functionalized for potassium sensing. Electrodes are interrogated with a small-signal sine wave and potassium-induced current signals are measured.

I. INTRODUCTION

IONS of potassium (K^+) and sodium (Na^+) are the main signal carriers in the nervous system. The difference in the concentration of both K^+ and Na^+ across the neuron cell membrane, as regulated by respective ion channels, plays a critical role in the propagation of action potentials, the spike-like signals neurons communicate with, as shown in Fig. 1(a). When the potential difference across the membrane is near its resting potential, the channels are closed. If for some reason (for example, due to influence by another neuron) the membrane potential increases to its threshold voltage, some channels begin to open [Fig. 1(a) (left)]. They let Na^+ ions into the cell causing fast cell membrane depolarization. This process continues until all channels in a small region are fully open causing membrane potential to rise sharply. Due to full membrane depolarization, Na^+ channels close. Next,

K^+ channels open. They carry K^+ ions out of the cell and quickly return the cell membrane potential to the resting state. This process repeats itself while propagating along an axon toward synapses which then carry the information encoded in the action potential to neighboring neurons.

Due to their significant role in the neuronal signaling, K^+ channel malfunctions are linked to over 100 neurological disorders, such as schizophrenia, Alzheimer's disease, spreading depression, and epilepsy. Selective real-time sensing of K^+ concentration (denoted as $[K^+]$) is therefore critical for the advancement of many neurological therapies.

Conventional intracranial electroencephalography (iEEG) does not measure $[K^+]$ as it cannot distinguish between K^+ and Na^+ ions. Experimental noninvasive techniques such as magnetic resonance imaging (MRI) have low accuracy, low resolution, and expensive [1]. Fluorescence sensing can be used to measure $[K^+]$ [2], [3] but requires fluorescent dyes. Fluorescent dye molecules are attached to potassium ions [3] and are used to track the changes in K^+ ions concentration utilizing long-wave radiation. This technique is not popular due to poor K^+ -to- Na^+ selectivity [3].

As opposed to fluorescence sensing or MRI, K^+ -amperometric techniques selectively monitor K^+ ion channel activity, as shown in Fig. 1(b). In the simplest case, when electrodes are small yielding small sensory currents, two electrodes, a working microelectrode (WE) and a reference microelectrode (RE) are utilized. (For larger sensory currents, when larger electrodes are used, a circuit known as a potentiostat is employed for this purpose, where a third counter electrode (CE) is introduced to conduct the higher current instead of RE, as needed to maintain constant electrochemical potential of the RE). A voltage is applied between the two electrodes to interrogate the sample, and the corresponding current is measured. The voltage waveform choice depends on the specific electrochemical sensing method used, such as sinusoidal for impedance spectroscopy, a periodic ramp for cyclic voltammetry, and a pulse for pulsed voltammetry. The recorded current contains information about the presence and the concentration of a specific biochemical target. Target-specific ionophores deposited onto the WE further improved the specificity. Existing amperometric techniques' biosensor arrays employing potassium ionophore monolayers [6]–[8] can be utilized to both improve ionic selectivity and increase spatial resolution of $[K^+]$ measurements. Conventional ionophore monolayers are prone to biofouling where biointerferers from the cerebrospinal fluid (CSF) attach to the biosensor surface and render the sensor array desensitized.

Many amperometric biosensor interface systems for various applications have been developed [4], [5], [7], [9]–[12]. In [10], a glucose monitoring system has been presented, where four carbon-nanotube-coated electrodes are used to monitor glucose levels in blood. The carbon nanotube structures are formed on a passive substrate and then stacked on a PCB that contains the electronic system. In [11], a biocompatible electronic sensor chip is implanted close to a tumor and is able to determine the oxygen content in a tissue under

test. It has only one biosensory site and offers no spatial information regarding oxygen concentrations. A tear glucose monitoring implant is presented in [7]. The biosensor and the integrated electronics are fabricated on a contact lens. The lens is also equipped with a magnetic coil for inductive powering and data telemetry. To reduce power consumption, the sensors are designed with a slow response of approximately 0.2 Hz. These biosensors do not provide any spatial sensitivity. Biosensors for the detection of pathogenic DNA for the applications have also been proposed [4], [5], [12]. Despite their promising features, the implantation of these biosensors have not yet been reported.

Typically, biochemical current sensing and impedance spectroscopy sensors are required to sense input currents in the range of pA to nA as this is the range of currents produced by ionic concentrations. The biosensors frequency response typically covers a range from 1 Hz to \sim 4 kHz as this is the bandwidth of current variations in electrophysiological measures (EEG, LFPs, ENG, etc.). In addition, for biomedical chronic implantation, the implanted devices have to consume ultralow power (sub-milliwatts). High-density microelectrode arrays are required to provide high-spatial resolution sensing.

We present a multichannel sensory microsystem for low-cost high-spatial-resolution impedance monitoring of $[K^+]$ in an animal brain *in vivo*, that addresses the design challenges of miniaturized implantable analog frontends. The design of the analog frontend presented here targets the main requirements of ultralow power and compact integration. It measures the ionic concentration of potassium which is an important representation of the neurochemical brain activity at the cellular level.

We utilize the impedance spectroscopy measurement technique as shown in Fig. 1(b), where K^+ - sensitive probe molecules are interrogated by applying a small (\sim 10 mV) sinusoidal voltage waveform onto the working electrode (WE), and the corresponding current I is measured. The resulting impedance is thus a selective measure of $[K^+]$ in the extracellular space ($[Na^+]$ is measured the same way, but yields a distinctly different impedance spectrum). Double-barrel glass electrodes are the gold standard for *in vivo* K^+ amperometry, but are bulky – thus have low temporal and spatial resolution, and are not implantable. Also, their slow response time makes them not suitable for sensing fast changes in concentrations and prevents them from capturing abrupt changes in $[K^+]$ which have been reported during an epileptic seizure and subsequent cortical spreading depression.

The focus of this manuscript is on the CMOS brain impedance spectroscopy integrated circuit (IC). The IC selectively senses K^+ (over Na^+) ions concentration by computing the complex impedance on an array of up to 12 electrodes. This article extends on an earlier report of the principle and demonstration in [13], and offers a more detailed analytical treatment of the operation of the opamp-less delta-sigma analog-to-digital converter (ADC) as well as additional experimental results. The rest of this article is organized as follows. Section II describes the developed technique of microelectrode functionalization with an antifouling layer for potassium ion selectivity. Section III discusses electrochemical

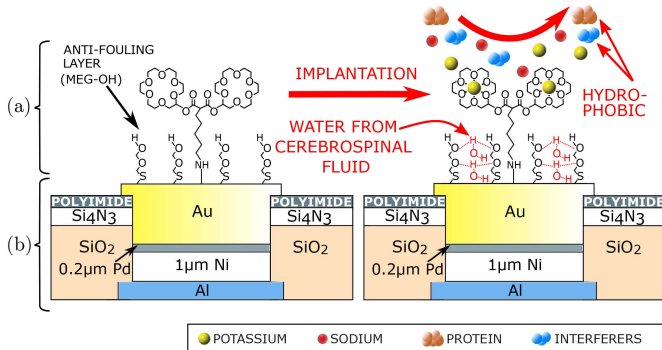


Fig. 2. Envisioned concept of the joint integration of (a) K^+ -sensitive fouling-resistant surface chemistry and (b) bio-compatible and CMOS-compatible microelectrode materials (Ni-Pd-Au metal stack), both located directly on the surface of a CMOS IC. This concept is validated in this article by implementing the K^+ -sensitive surface chemistry on a passive gold microelectrode, not on CMOS. We have previously experimentally proven fabrication and functionality of a biocompatible Ni-Pd-Au metal stack on CMOS top metal (Al) [4], [5].

impedance spectroscopy (EIS) systems, compares between different impedance analysis techniques, and highlights the principle of operation of the proposed impedance extraction system. Section IV presents the essence of the opamp-less delta-sigma loop operation with a passive integrator. In Section V, the proposed sensing channel characterization is detailed and *in vivo* validation of the system is presented.

II. ANTI-FOULING LAYER

The proposed ion-sensitive electrode functionalization technique is envisioned to be implemented on top of CMOS top-metal aluminum pads as shown in Fig. 2, as described in this section.

Biofouling of potassium-sensitive electrode surface by bio-contaminants (e.g. proteins and lipids) and other hydrophobic interferers over time is one of the major challenges that faces the implantation of biosensing microelectrodes *in vivo*. The complexity of biofouling stems from the fact that some organic contaminants get attracted to the ionophore molecules on the electrode surface and hence impair the electrode functionality. In an ideal case, where there are no contaminants in the electrode surroundings, only potassium ions bond with the ionophore molecules are found.

In the presented sensors, as shown in Fig. 2(a), we have also developed a method to deposit a mixed ultrathin surface monolayer onto a gold surface [14] to both provide sensitivity to K^+ in the CSF and to minimize interference caused by protein and other interferers adsorption. The two modified K^+ -binding crown ethers [the cyclic chemical compounds in Fig. 2(a)] capture K^+ ions and as a result modify the surface impedance. This process is reversible. An antifouling layer is added to prevent the proteins and other floating organic molecules from getting attached to the electrode surface. Using such a layer, when the electrodes are implanted, the water molecules bond with the MEG-OH branches, such that the electrode surface becomes protected from hydrophobic interferers such as proteins and lipids. In such a case, the electrode surface is selectively sensitive to potassium ions

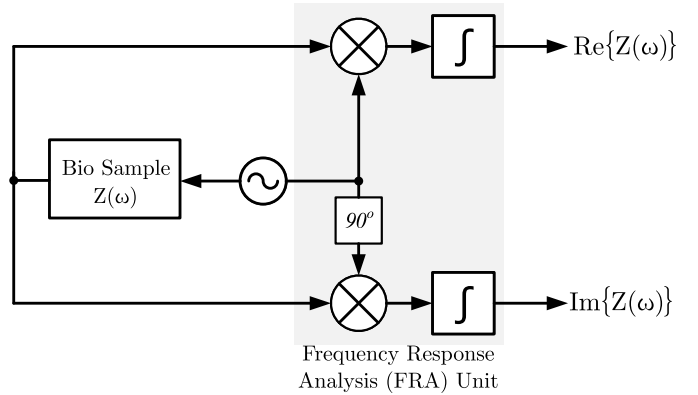


Fig. 3. Conventional FRA block diagram.

for subsequent impedance-based measurements of its concentration. When compared with conventional probe-based techniques, the electrode surface does not undergo significant changes after implantation. The impedance changes only when $[K^+]$ changes, and not as a result of interferers attaching themselves to the electrode.

In the extracellular space, sodium ions are also present in the test sample. To differentiate between sodium ions and potassium ions, the system uses the fact that the impedance response for potassium ions and the sodium ions is different when they interact with the antifouling layer. Therefore, calibration curves for potassium ions and sodium ions are obtained by varying the $[Na^+]$ and $[K^+]$ concentrations in an artificial CSF solution. These calibration curves are then used to differentiate between potassium and sodium concentrations during the actual measurement *in vivo*.

Fig. 2(b) shows how the antifouling layer can be implemented on CMOS top-metal aluminum pads. Aluminum sensory pads are plated with Ni/Pd/Au to make the surface inert and biocompatible. We have previously experimentally demonstrated this in [4] and [5].

III. IMPEDANCE SPECTROSCOPY

In state-of-the-art EIS systems, two main techniques are implemented and widely used: fast Fourier transform (FFT) and frequency response analysis (FRA). FFT is a processing-intensive computational method that employs complex digital algorithms, making it power-hungry and requiring large silicon area. In contrast, FRA can be implemented using less power and smaller silicon area. Fig. 3 illustrates the conventional implementation of FRA.

The sample being tested is interrogated by a sinusoidal function. Then the output of the sample is multiplied separately by two sinusoidal waves: one having the same phase as the interrogation signal, and one with a 90° phase shift. The output of both multiplication processes is integrated over one cycle to produce the real and imaginary parts of the impedance. When repeating the same procedure over a range of frequencies, the outputs of the FRA unit represent the real and imaginary parts of the sample impedance frequency spectrum.

State-of-the-art implementations of FRAs perform the multiplication and integration in the digital domain (after the

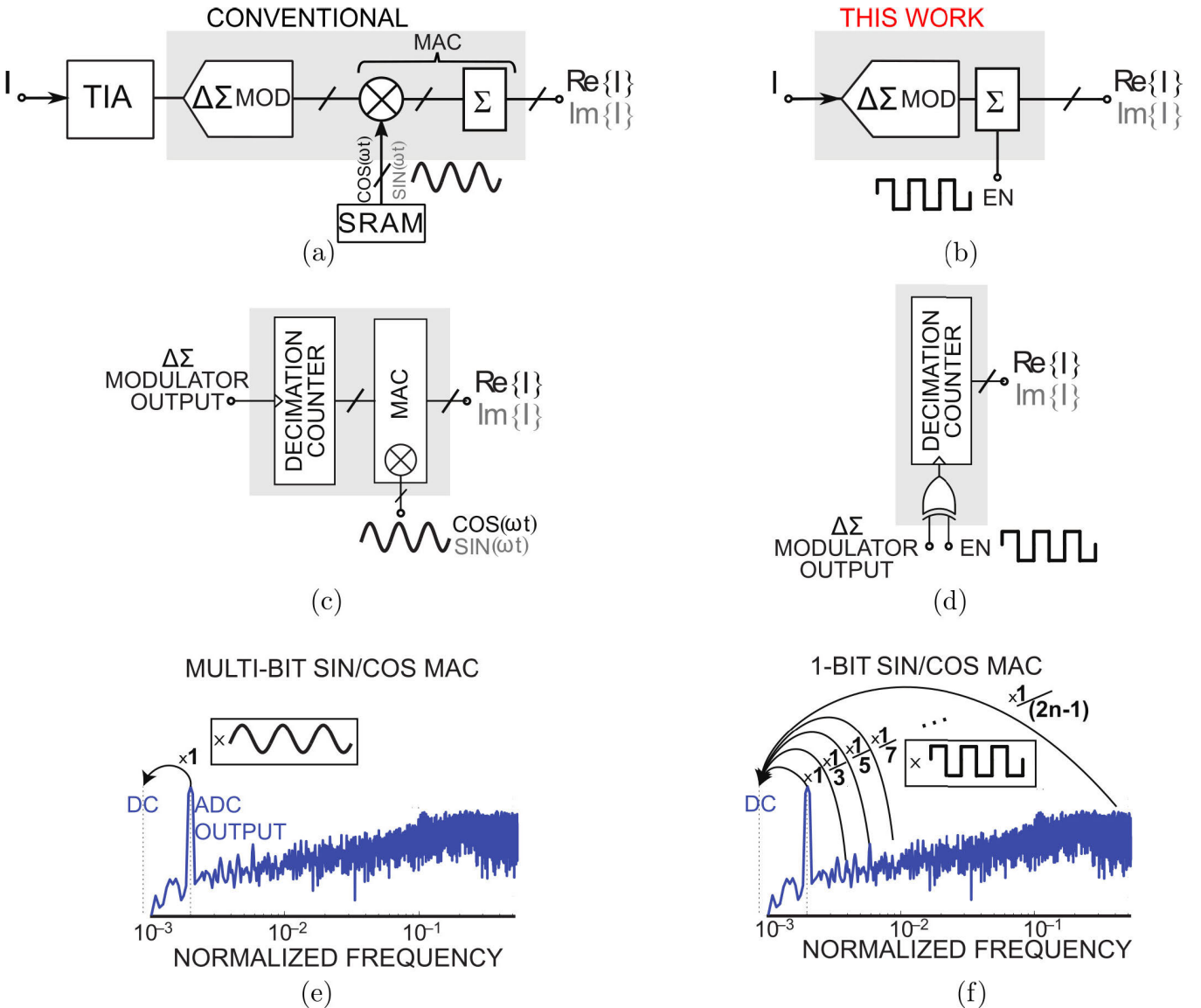


Fig. 4. Impedance extraction system reduction: unlike conventional analog front ends (a), the TIA and ADC are combined into a current-input opamp-less $\Delta\Sigma$ ADC (b). Cosine and sine multiplication and accumulation (MAC) (c) are replaced by a simple XOR logic gate performing square wave multiplication (d). As opposed to the ideal multiplication spectrum (e), the 1-bit multiplication leads to harmonics contributing to the output (f), but as their amplitude drops inversely proportionally to the frequency, the resulting error remains below 2%.

ADC), in the analog domain, or by integrating both of these operations within a multiplying ADC, such as a multiplying dual-slope ADC [9].

A typical implementation of digital multiplication is depicted in Fig. 4(a), where it is performed on the output of the ADC. The example shown includes a $\Delta\Sigma$ ADC, as it is a popular choice due to the low bandwidth required for biomedical signals and hence, lower sampling rates and the noise shaping property yielding a high SNR [15]. The digital representations of $\sin(\omega_o t)$ and $\cos(\omega_o t)$ are usually stored in memory and fed to a power- and area-inefficient multibit digital multiplier followed by an accumulator, i.e. multiply and accumulate (MAC) operation [Fig. 4(c)]. This process implies a need for static random-access memory (SRAM) storage as well as routing the digital coefficients to every readout channel in the system. In case of very low-frequency impedance

analysis, one way to save power in this implementation at the expense of some system complexity is the reuse of a single MAC operation and alternating *sin* and *cos* signals, together with time multiplexing, to extract the real and imaginary components of the impedance sequentially. In this case, proper selection of sampling and multiplexing frequencies is crucial. Also, flushing of the registers in the accumulator has to be fast enough to avoid any interference between the two accumulation processes.

Fig. 4(b) shows the principle of operation of the proposed impedance spectroscopy technique. A delta-sigma ADC with a high over sampling ratio (OSR) has been utilized to achieve a high SNR. Thanks to the narrow frequency bandwidth of the input signals, the dynamic power of the ADC can be kept low, despite the high OSR value. The noise shaping property of $\Delta\Sigma$ ADCs results in modulating the noise from low frequency to

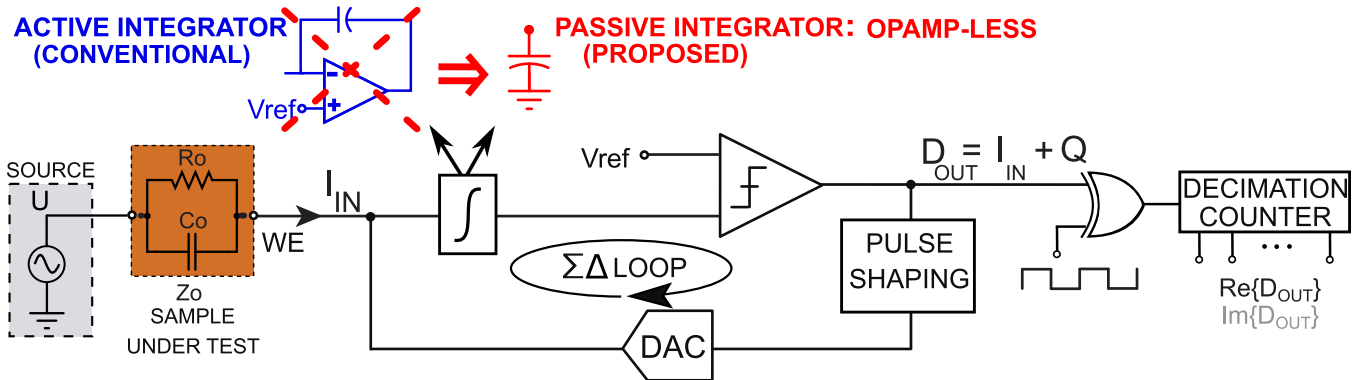


Fig. 5. Opamp-less $\Delta\Sigma$ -modulated ADC implementation: a conventional TIA integrator is replaced with a large capacitor as a passive integrator. The ADC output is multiplied by a square wave using a simple XOR gate.

higher frequencies and the quantization noise to be much lower than Nyquist-rate ADCs at low frequencies (baseband). In the proposed FRA scheme, the ADC output multibit multiplication by sinewave coefficients [Fig. 4(c) and (e)] is replaced with a single-bit squarewave multiplication [Fig. 4(d) and (f)]. Replacing the high-resolution sinewave by its 1-bit squarewave representation causes additional spectral components due to the harmonics of the squarewave as shown in Fig. 4(f). Due to the nature of the square wave, where the weight of its harmonics decreases hyperbolically with frequency, the strong $\Delta\Sigma$ high-frequency noise harmonics do not significantly corrupt the output result of the multiply-and-accumulate operation, allowing the system to take advantage of the low-noise baseband, leading to a higher sensitivity when compared with conventional implementations. Hence, the real and imaginary components of Z are efficiently computed by using a single-bit square wave, and a 90°-delayed version of it, instead of $\sin(\omega_o t)$ and $\cos(\omega_o t)$ functions. This eliminates the need to store these functions in a large and power-consuming SRAM. Even more importantly, this also eliminates the area and energy requirements of a multibit multiplier and adder, which are prohibitive for implantable applications. In this case, the reuse of a single MAC operation using time multiplexer becomes unnecessarily complicated in this scheme, as simultaneous extraction of the real and imaginary components comes with using only a single XOR gate and a counter.

IV. OPAMP-LESS $\Delta\Sigma$ ADC

The development of the biocompatible antifouling layer, discussed in Section II, enables chronic implantation of the proposed impedance spectrum analyzer. Chronic implantation of biosensory devices is necessary for long-term studies, which dictates specific requirements on the implanted device, such as biocompatibility to avoid any tissue-implant reaction, small form factor, high level of integration, and ultralow power consumption. While biocompatibility is taken care of by virtue of the presented antifouling layer, low power consumption and high integration level are ensured by the novel channel architecture presented in this section.

For biochemical sensing, amperometry is required for measuring ion concentrations. Typically, a transimpedance amplifier (TIA) is employed to provide a minimal input impedance and to maintain the input node voltage level unchanged

during current sensing. For these two requirements, a negative feedback loop is necessary to set the virtual ground at the input node of the readout circuit while providing the required low input impedance. Conventionally, an amplifier (usually an opamp/OTA) with a passive feedback network is used to perform this function. To have the sufficient gain and bandwidth for maintaining the feedback, 30% to 50% of the readout circuitry power budget is consumed in the amplifier [4], [5], [9], [16], whereas the rest of the power budget is divided among ADC, digital signal processing, and biasing circuitry. A major power reduction can be achieved if the negative feedback is maintained without the use of an amplifier.

In the case of a delta-sigma ADC, an integrator is included in the negative feedback loop to accumulate the $\Delta\Sigma$ loop error and to produce an output bit stream that resembles the analog input after decimation. In the presented channel, we eliminate the opamp and replace the loop integrator by a large capacitance C_{INT} , in the way depicted in Fig. 5. This opamp-less $\Delta\Sigma$ negative feedback loop is used to maintain a low input impedance and to set the virtual voltage at the input node. The difference between the feedback and the input currents is integrated on C_{INT} , while the voltage at C_{INT} , which is also the input node, is set by the loop comparator reference voltage V_{REF} (Fig. 5). Since a capacitor has a very high impedance at low frequencies, the feedback loop gain is preserved for low-frequency input signals, which is well suited for biomedical applications. Provided that the loop is fast enough to track the voltage variations at the input node (on C_{INT}) caused by fast or relatively large input currents, the operation of the loop is maintained and the input node is set at V_{REF} . This is achieved by choosing high sampling frequency when compared with the input frequency as well as other conditions that are detailed in Section IV-B.

In addition, as indicated in Section III, the $\Delta\Sigma$ output stream allows to perform the MAC operation inside the ADC itself by replacing the multibit sin/cos multiplication with area- and power-efficient single-bit squarewave multiplication [Fig. 4(b), (d) and (f)].

A. Passive Integrators

As mentioned earlier in this section, a fundamental building block in $\Delta\Sigma$ ADCs is the integrator (or the loop filter),

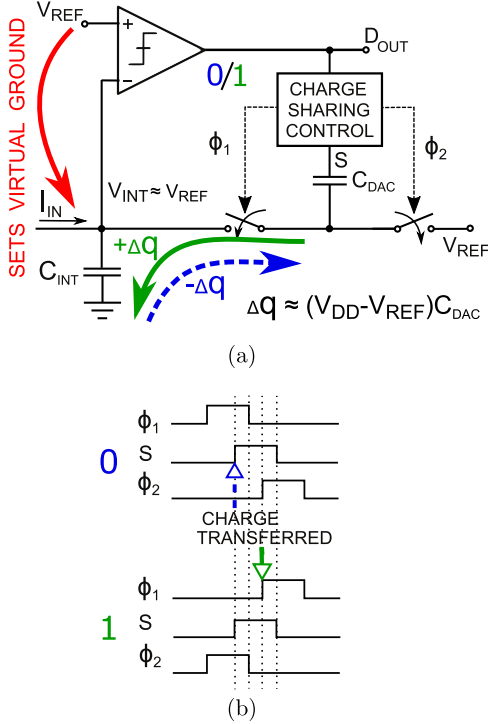


Fig. 6. First-order $\Delta\Sigma$ -modulated ADC operation phases. ADC feedback loop maintains the current input node as a virtual ground. (a) Loop compensates input currents by pushing/pulling charge from the input passive integration capacitor according to comparator decision. (b) Clock edges at which the charge pushing/pulling occurs.

as it performs the function of $\Delta\Sigma$ loop error accumulation. Conventionally, for continuous-time $\Delta\Sigma$ loops, integrators are implemented as active filters, using RC sections and opamps, or g_m -cells (G_m -C circuits). In discrete-time $\Delta\Sigma$ converters, the loop filter is implemented using switched capacitor integrators, which use OTAs for charge integration. In both cases (opamps and G_m -C circuits), high linearity is an important design specification that has to be maintained. In CMOS technologies, the realization of highly-linear power-efficient active filters or switched capacitor integrators is getting more and more challenging with short channel transistors. On the other hand, the performance of digital building blocks and switches is improving. It bodes well for over sampling ADCs, $\Delta\Sigma$ in our case, to employ passive switched-capacitor filters and integrators, where the MOS transistor is only used as a switch. A switch works better at higher frequencies as compared with active filters and G_m -C circuits, where the maximum operating frequency is limited by the opamp settling. Also, the input-referred noise of a passive switched-capacitor filter is expected to be lower as it only employs one input capacitor. It also exhibits higher linearity due to passive operation [17].

B. First-Order Opamp-Less $\Delta\Sigma$ ADC

Fig. 6 illustrates the operation phases of the implemented opamp-less channel. A charge-sharing DAC pushes/pulls charge through a small capacitor C_{DAC} to/from the much larger integrator input capacitor C_{INT} , depending on the comparator output. A high OSR is selected so that the digital feedback loop maintains V_{INT} approximately equal to V_{REF} .

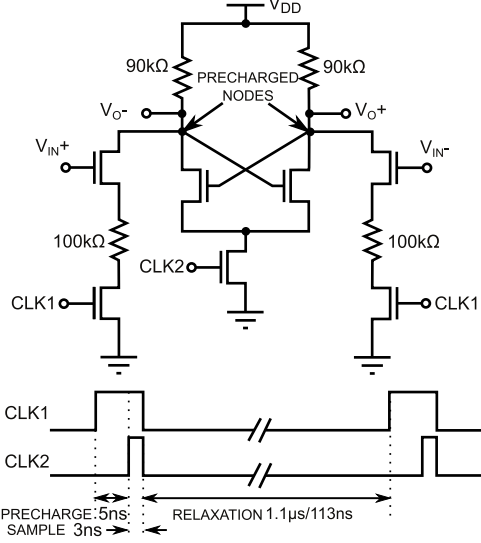


Fig. 7. $\Delta\Sigma$ ADC comparator implementation. $100\text{ k}\Omega$ degeneration resistors are used to further reduce the effect of hysteresis and path dependence on the performance. Low-duty-cycle sample (clk 1) and decision (clk2) clocks are used for power saving.

The OSR has to be high enough to keep the change in V_{INT} with respect to the reference voltage V_{REF} smaller than the voltage change caused by the smallest desired input current ($I_{in,min} \times T_S/C_{INT}$). The input current is integrated directly by the input capacitor C_{INT} leading to a voltage range smaller than that on the conventional opamp feedback capacitor, but this does not increase susceptibility to comparator noise. This is because the opamp-less ADC rejects dc offset and 1/f noise because, as proven later in this section, its transfer function is approximately equivalent to that of an active-integrator $\Delta\Sigma$ ADC. Hence, inputs to the $\Delta\Sigma$ loop before the integrator will experience a low-pass signal-transfer function (STF). For inputs that enter the loop after the integrator, they will experience a high-pass signal-transfer function similar to the quantization noise-transfer function (NTF). Since the comparator noise is generated in the loop after the integrator, it is modulated to high frequencies together with the quantization noise [18].

The comparator circuit is depicted in Fig. 7. It consists of a regenerative latch circuit with $90\text{ k}\Omega$ drain resistors and input sampling transistors with $100\text{ k}\Omega$ degeneration resistors. The values of these resistors were selected to minimize power consumption at sampling and regeneration instants while maintaining adequate accuracy and speed. Resistive degeneration mitigates path dependence and hysteresis. The dynamic/transient power consumption (P_t) of the comparator is proportional to V_{DD}^2 ($P_t \approx f_s \cdot V_{DD}^2 \cdot C$). It is greatly reduced by operating at low supply level of 0.6 V. The static power consumption, due to the direct-path current, (P_{DP}) is mainly caused by direct currents between the supply and the ground during input sampling and decision phases. Therefore, the width of the sampling pulse (CLK1) and decision pulse (CLK2) are minimized (8 and 3 ns, respectively) and the drain and degeneration resistors are increased and optimized to help reduce the direct current path power dissipation.

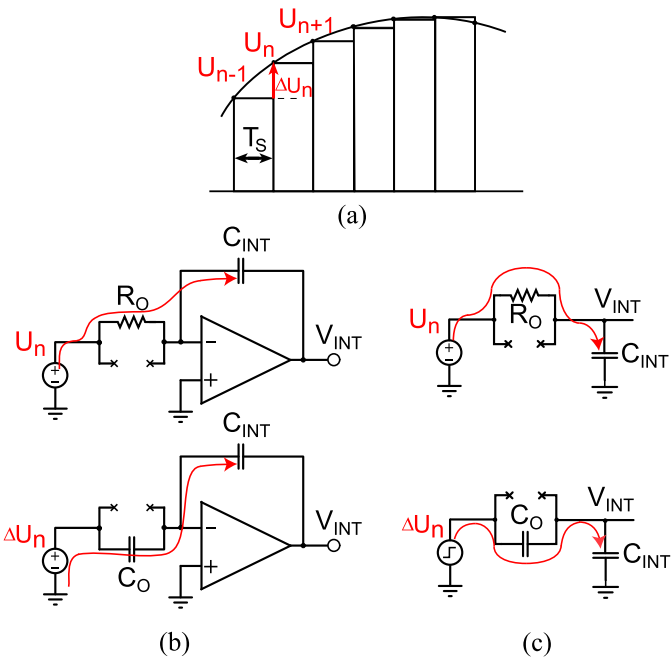


Fig. 8. (a) Low-frequency input signal is dissected into infinitesimal pulses using FEM approximation. Input signal is approximated into a dc signal U_n and small pulses ΔU_n . (b) and (c) compare the responses of conventional active integrator circuits, in (b), and the presented passive integrator circuit, in (c), to the two input signal components.

To demonstrate the effect of using a passive integrator, as compared with using an active integrator, on the system-transfer function, a simplified analysis is done on both active and passive integrators as shown in Fig. 8. Since the **bandwidth of the input signal is very low** when compared with the sampling frequency of the **oversampled $\Delta\Sigma$ ADC**, the problem is analyzed using finite element method (FEM), as shown in Fig. 8(a). The input signal is divided into small infinitesimal samples with T_S widths. Based on this assumption, the input signal at each sample n consists of two components: a dc component U_n and a step function ΔU_n .

For an active integrator shown in Fig. 8(b), the two input components affect the integrator output in different manners. The dc component U_n charges the integrator capacitance C_{INT} through the resistor R_o , whereas the step function ΔU_n charges C_{INT} through the capacitor C_o . The output voltage of the integrator V_{INT} at the end of each sample is represented by the following equation, ignoring the minus sign of the inverting amplifier configuration:

$$\begin{aligned} V_{INT,n} &= V_{INT,n-1} + U_n \cdot \frac{T_S}{R_o C_{INT}} + \Delta U_n \cdot \frac{C_o}{C_{INT}} \\ &= V_{INT,n-1} + \alpha U_n + \beta \Delta U_n \end{aligned} \quad (1)$$

where α is the ratio between the sampling time T_S and the circuit time constant $R_o C_{INT}$; and β is the ratio between C_o and the integration capacitance C_{INT} . Fig. 8(c) shows the same analysis applied on the passive integrator, resulting in the following equation:

$$\begin{aligned} V_{INT,n} &= V_{INT,n-1} \cdot e^{-\frac{T_S}{R_o C_{INT}}} + U_n \left(1 - e^{-\frac{T_S}{R_o C_{INT}}}\right) \\ &\quad + \Delta U_n \cdot \frac{C_o}{C_o + C_{INT}} \end{aligned} \quad (2)$$

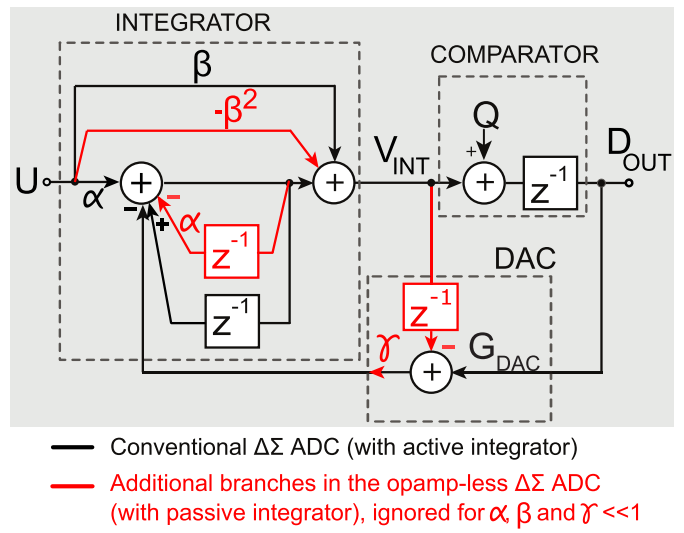


Fig. 9. Canonical form of first-order $\Delta\Sigma$ ADC. Conventional $\Delta\Sigma$ ADC branches are black and branches added as a result of using the passive integrator are marked in red. The red branches can be ignored for α, β , and $\gamma \ll 1$.

By increasing C_{INT} to be large enough to satisfy the requirement of proper integration (much larger than C_o), and reducing T_S to be much smaller than the time constant $R_o C_{INT}$, (2) can be reduced to the following equation:

$$\begin{aligned} V_{INT,n} &= V_{INT,n-1} - V_{INT,n-1} \cdot \frac{T_S}{R_o C_{INT}} + U_n \cdot \frac{T_S}{R_o C_{INT}} \\ &\quad + \Delta U_n \cdot \frac{C_o}{C_{INT}} \left(1 - \frac{C_o}{C_{INT}}\right) \\ V_{INT,n} &= V_{INT,n-1} + \alpha U_n + \beta \Delta U_n - \alpha V_{INT,n-1} \\ &\quad - \beta^2 \Delta U_n. \end{aligned} \quad (3)$$

As derived in (3), the use of a passive integrator introduced two new terms when compared with (1) of an active integrator which are $\alpha V_{INT,n-1}$ and $\beta^2 \Delta U_n$.

Fig. 9 shows the superimposed z-domain models of both the conventional active integrator (black) and the presented $\Delta\Sigma$ ADC (black and red). As discussed, removing the opamp causes two additional branches with the weights α and β^2 to appear. The absence of a TIA causes the 1-bit DAC to have an additional unwanted branch connecting it to the comparator input. The two designs become approximately equivalent when the coefficients α , β , and γ are all $\ll 1$. This is true when: 1) the sampling period is negligible when compared with the time constant of the tissue-electrode interface; 2) C_{INT} is much greater than the equivalent shunt capacitance of the microelectrode; and 3) the input current is much smaller than the full-scale input current of the ADC. In the context of *in vivo* potassium amperometry, condition (1) is satisfied when the ADC operates at sampling frequencies in the megahertz range (above 800 kHz) for the input bandwidth of a few kilohertz (5 kHz). Condition (2) is met by keeping size of the WE small ($\simeq 50 \mu\text{m} \times \simeq 100 \mu\text{m}$). C_{INT} is the MIM capacitor which shields the WE from underneath, thus the WE capacitance is effectively equal to the fringe capacitance between the WE and the adjacent reference electrode.

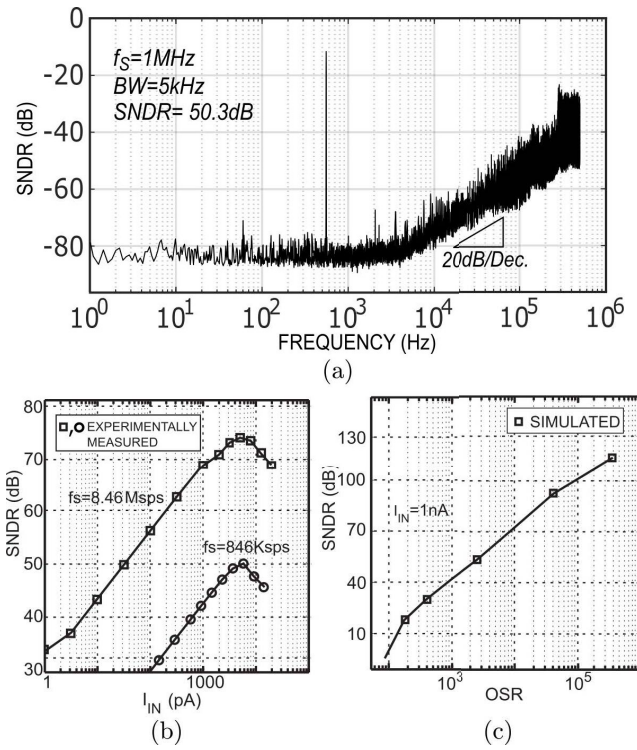


Fig. 10. Experimentally measured and simulated characterization of the opamp-less $\Delta\Sigma$ ADC SNDR. (a) FFT spectrum of the $\Delta\Sigma$ output stream, (b) SNDR plots versus inputs current levels at two different clock frequencies, and (c) SNDR versus OSR.

It has to be noted that although the elimination of the opamp from the system has reduced the power consumption severely when compared with other systems, it also comes with some drawbacks that had to be very carefully mitigated by accurately selecting proper design choices of sampling frequency, electrode sizes, suitable input range, and measuring environment. These drawbacks, such as lack of linearity at high input frequencies and amplitudes, are mitigated by increasing the OSR. Due to the nature of the feedback single-bit DAC, increasing the OSR leads to increasing the rate of charge sharing at the integrator capacitor which in turn leads to increasing the feedback loop gain. Hence, for higher frequencies, the same linearity and SNR levels as the opamp-based designs are achieved at the expense of high dynamic power. Susceptibility to large artifacts is also overcome. Since the ADC architecture is continuous-time $\Delta\Sigma$, intrinsic anti-aliasing filter and low-pass filter-transfer functions are incorporated. In case of high-frequency artifacts, they will be filtered out by these filters. If they are at low frequencies and have large amplitudes enough to saturate the passive $\Delta\Sigma$ ADC input circuit, they will saturate any opamp-based circuit as well. Various precautions have been made to ensure proper measurement results, such as electrodes size optimization, shielding, and encapsulation of the IC.

V. EXPERIMENTAL RESULTS

Fig. 10(a) shows the FFT spectrum of the output $\Delta\Sigma$ ADC stream. The channel achieves an signal-to-noise-and-distortion ratio (SNDR) of 50.3 dB at 1 MHz sampling frequency over

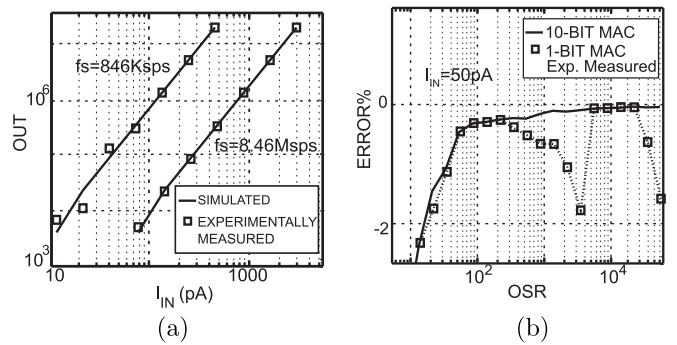


Fig. 11. Experimentally measured characterization of the opamp-less $\Delta\Sigma$ ADC. (a) ADC Digital output versus input current levels. (b) Impedance calculation errors compared to a 10-bit multiplying ADC output.

5 kHz bandwidth. Fig. 10(b) shows the SNDR plot of the ADC at two sampling frequencies: 846 ksps and 8.46 Msps. The latter yields a higher dynamic range, due to an increased range of currents that can be pushed/pulled by the DAC. Fig. 10(c) shows that the OSR improves the SNDR by ~ 28 dB/decade.

Fig. 11(a) depicts the ADC output versus the input current at the two sampling frequencies. The experimental results differ from the simulated results for small currents as this is near the 1 pA sensitivity. Fig. 11(b) shows the error in the digital impedance output using both a 10-bit sine wave and its 1-bit (square wave) approximation. For OSR of 500 or more, the computation error is less than 2%.

The IC was validated *in vivo* in an anesthetized immobilized mouse. The IC was mounted on a flexible polyimide electrode array shown in Fig. 12, with its four sensory gold strips chemically functionalized as shown in Fig. 2. The chip pads are wire bonded to the soldering pads of the microelectrode array. The IC is, then, covered by epoxy. The remaining area of the solder pads, not covered with epoxy, is used to connect the chip signals to the benchtop instruments. This sensor array was then placed on a section of the cerebral cortex of a mouse exposed by craniotomy.

Fig. 13 depicts experimentally measured calibration curve for both $[K^+]$ and $[Na^+]$. As shown, the responses of the antifouling microelectrodes to sodium and potassium ions are distinguishable. These curves are obtained by varying the concentrations of K^+ and Na^+ in an artificial CSF solution. The electrode pad capacitance (C_S) is measured using the same impedance extraction architecture described in Section III. The potassium and sodium concentrations are increased equally as depicted in Fig. 13 (a) (2.5, 4.5, 6.5, and 10 mM). At each concentration level, an interrogation voltage of $8\text{ mV}_{\text{p-p}}$ is swept across frequencies from 100 Hz to 1 kHz on the solution [Fig. 14(a)]. The current output is recorded using the ADC [Fig. 14(b)]. As seen in Fig. 14(b), the current magnitude increases when interrogation frequency increases as the capacitance impedance reduces $[1/(j\omega C_S)]$, while the phase of the current signal has a 90° -phase shift with the voltage signal. The capacitance of the microelectrode pads (C_S) changes much more for changes in $[Na^+]$ than for $[K^+]$ changes. The concentration range of potassium from 2 to 10 mM has been measured by the presented EIS channel that

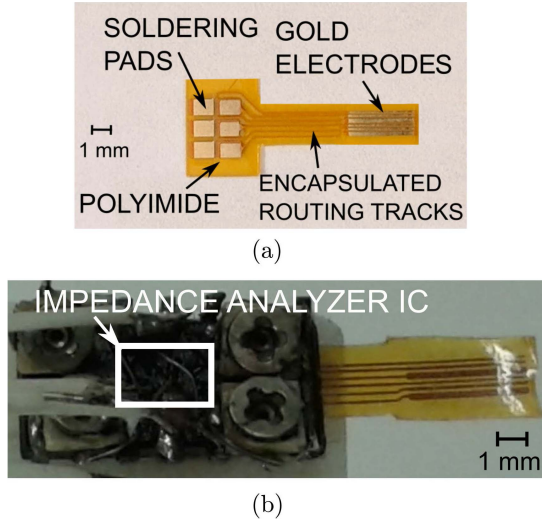


Fig. 12. (a) Four-channel gold microelectrode array implemented on a polyimide substrate (four out of the six contacts are used). (b) Connection between the IC and the polyimide flexible electrode.

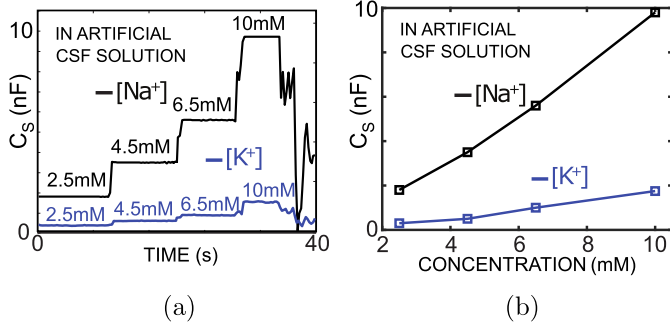


Fig. 13. Potassium and sodium concentrations calibration curves. (a) Electrode pad capacitance (C_s) versus time and (b) C_s versus concentration. C_s changes much more for changes in $[Na^+]$ than $[K^+]$ changes.

has a dynamic range of 1 pA–20 nA with a bandwidth of 5 kHz. This range includes the typical range of these ions concentration in a nonpathological brain.

A block diagram of the *in vivo* experimental setup is shown in Fig. 15(a). The mouse brain cortex is subjected to optogenetic stimulation pulses [14]. The impedance analyzer IC is mounted on the polyimide flexible substrate [Figs. 12(b) and 15(b)]. The outputs from the four-channel microelectrode and the reference glass electrode are stored in an off-chip memory for display and comparison.

Fig. 16 shows $[K^+]$ concentration measured *in vivo* in an anesthetized mouse during pulsed optogenetic stimulation (under an ethics protocol at Toronto Western Hospital). In Fig. 16(a), the $[K^+]$ variation recorded by a double-barrel glass electrode inserted in the cortex layer 2–3, serving as a control signal for comparison, is shown.

Fig. 16(b) depicts the impedance of the gold microelectrode placed on the brain cortex, recorded by the $\Delta\Sigma$ ADC simultaneously with the control signal. To record real-time $[K^+]$ variation by gold microelectrodes, an 8 mV peak-to-peak sinusoidal voltage generated off-chip is swept across

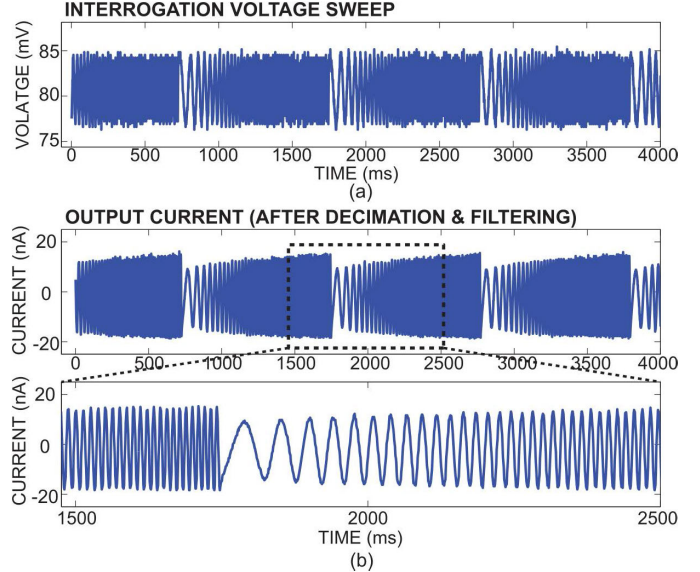


Fig. 14. Frequency sweep for impedance spectroscopy. (a) Interrogation voltage signal frequency sweep from 20 Hz to 5 kHz. (b) Output current from ADC after decimation and filtering.

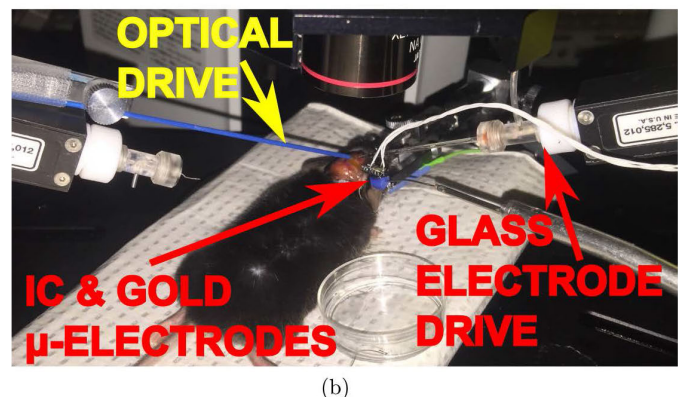
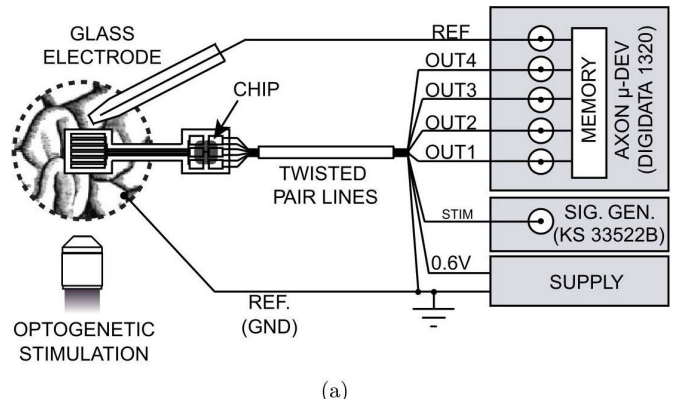


Fig. 15. *In vivo* measurement setup. (a) Block diagram of *in vivo* channel measurement setup and instruments. (b) Measurement setup of the experiment done on an anesthetized mouse. Optogenetic stimulation pulses are applied to the brain cortex. A twisted pair wires are used to connect the IC to the off-chip instruments to minimize interference.

frequencies, from 100 Hz to 1 kHz. The resulting current is recorded by the $\Delta\Sigma$ ADC and processed by a reconstruction algorithm that extracts the R and C parameters of the series

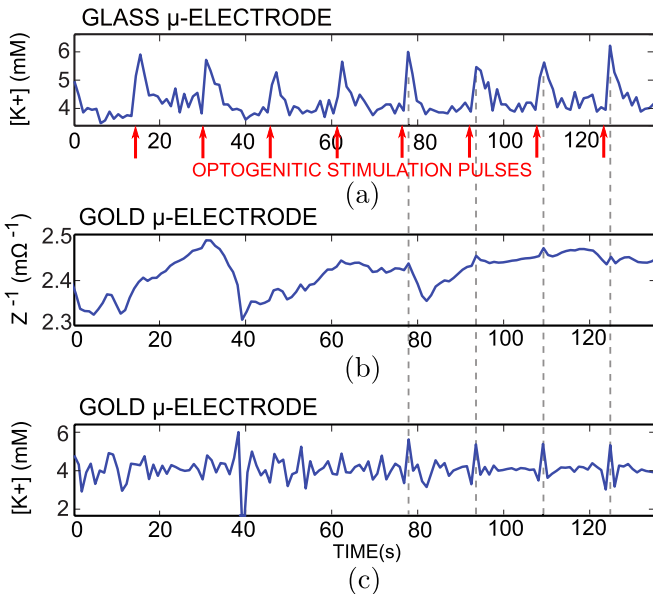


Fig. 16. Experimentally measured *in vivo* results from an anesthetized mouse cortex: (a) $[K^+]$ recording using a conventional double-barrel glass electrode, (b) sample impedance using gold μ -electrode, and (c) $[K^+]$ computed based on the measurements in (b).

RC model as shown in Fig. 5. The resulting impedance is plotted in Fig. 16(b).

Fig. 16(c) shows real-time $[K^+]$ values extracted from this electrode impedance by the reconstruction algorithm using the calibration curve in Fig. 13. The reconstruction algorithm is implemented in MATLAB, and executed in real time and in parallel with the *in vivo* measurements. The algorithm function is the first to add the real and imaginary parts of the extracted impedance, point by point. Then, the impedance is converted to admittance in the form of parallel R_p and C_p . For every measurement point, the extracted capacitance C_p is compared to lookup table of the electrode pad capacitance C_s derived from measurements shown Fig. 13(b). The capacitance caused by sodium is then subtracted and the resultant capacitance is compared to potassium curves for concentration values. This process takes few milliseconds that it does not affect the real-time measurements. In Fig. 16, it is clear that after the time $t = 70$ s, the reconstructed $[K^+]$ data from the algorithm show photogenetically induced $[K^+]$ responses that peak at the same instances as the reference double-barrel electrode. However, the $[K^+]$ peaks recorded by the gold microelectrodes have more high-frequency information than those recorded by the double-barrel electrode. We hypothesize that this is due to the wider bandwidth of presented approach as compared with the conventional double-barrel electrode which are slow due to their large capacitance. Before the time $t = 70$ s, the response from the gold electrode array is not as pronounced as that of the glass electrode. This is likely because the interrogating volumes of the two electrode types are different. First, the glass electrode is inserted in cortical layers 2–3, and the gold electrode records at the cortex surface.

Second, the two electrode types cannot be colocated due to physical limitations of size and test setup configuration; thus, they are located at different coordinates, a significant distance

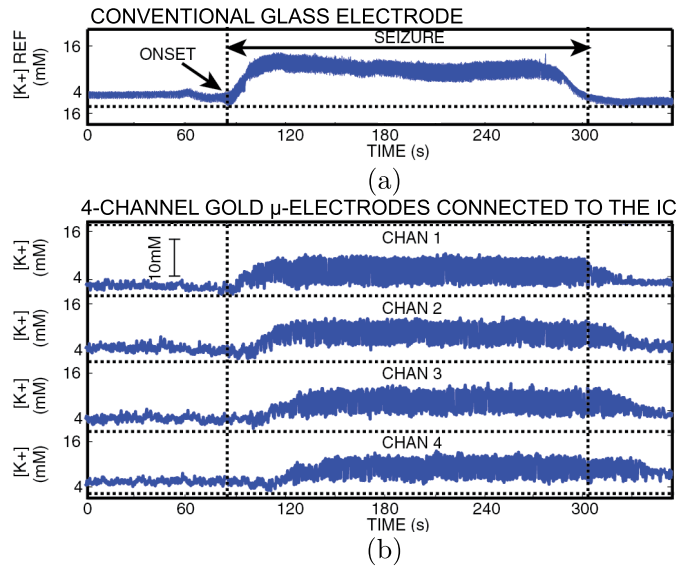


Fig. 17. Experimentally recorded *in vivo* $[K^+]$ levels during an epileptic seizure-like event in the mouse brain using (a) conventional glass electrode and (b) 4-channel gold electrode.

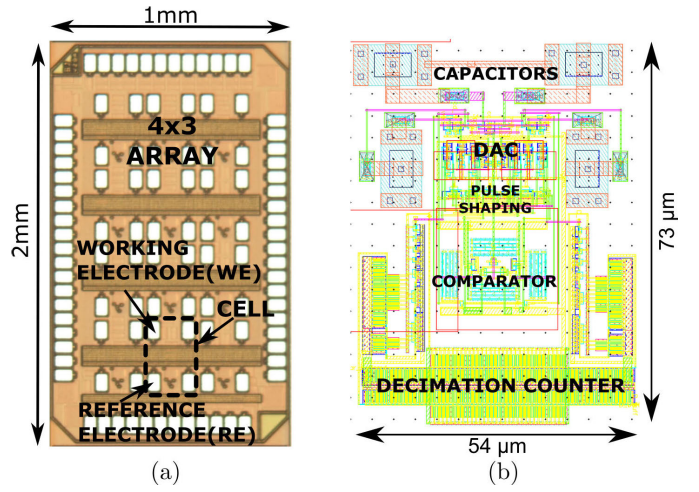


Fig. 18. (a) Die photograph of the 12-channel IC prototyped in a 130 nm CMOS process, showing reference electrode/pad (RE), WE and the single channel cell. (b) $\Delta\Sigma$ ADC channel layout including comparator, DAC, counter and pulse shaping blocks.

apart. As a result, the same effect from the optogenetic stimulation cannot be ensured at the beginning of stimulation but the effect tends to propagate and become more uniform after some time.

Potassium concentration measured by four gold electrodes during an induced epileptic seizure is shown in Fig. 17(b). The recordings are consistent with those obtained by a conventional glass electrode [Fig. 17(a)]. The potassium concentrations appear to drop slightly at the onset of a seizure. This drop is followed by an increase of approximately 10 mM at the onset. The $[K^+]$ concentration stays high during the seizure and then returns to normal levels after the animal is back to the normal state. Au electrode yields a significantly higher temporal resolution than what is currently attainable by the glass electrode.

TABLE I
TABLE OF COMPARISON

Reference	[19] TBioCAS 2007	[12] ISSCC 2008	[4] JSSC 2014	[7] JSSC 2014	[20]* VLSI 2015	[21] TBioCAS 2016	[22]* ISSCC 2016	[23]* ISSCC 2018	This Work
Technology [μm]	0.5	0.18	0.13	0.13	0.065	0.35	0.065	0.065	0.13
No. of Channels	16	24	54	1	1	1	1	1	12
Bandwidth [Hz]	4000**	-	3400	0.2	2M	4880	10M	3000	5000
Sensitivity [pA]	0.1	97	8.6	20	N/A	55	N/A	-	1
SNDR [dB]	50	70‡	56.5	-	69.1	72.1	72.2	65.5	50.3
Area/Ch. [mm²]	-	0.03*	0.06	0.22	0.013	0.111	0.027	-	0.004
Power/Ch. [W]	3.4 μ	-	8 μ	500 n	2560 μ	9.5 μ	1570 μ	180 n	50 n

“-” : Not Available “N/A”: Not Applicable

* Passive $\Delta\Sigma$ ADC

** Estimated

‡ External 5nF capacitor used at the input

The bold font denotes the best performance indicator in each row, where appropriate

SYSTEM POWER BREAKDOWN

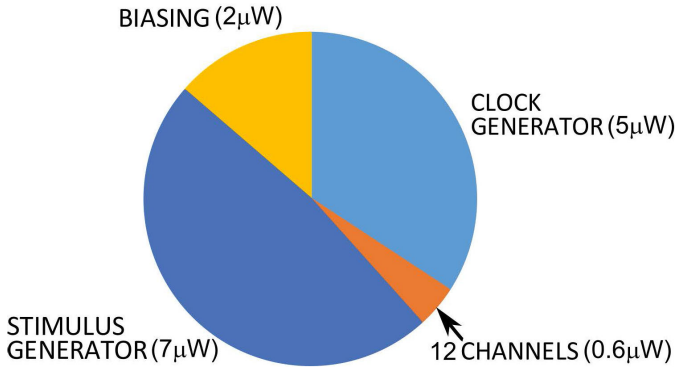


Fig. 19. System power breakdown. The overall system power is 14.6 μW .

Table I compares the presented circuit performance metrics with the state of the art. For EIS systems, each application has different requirements in terms of bandwidth, dynamic range, and sensitivity. Table I provides a comprehensive view of their performance. This design has the advantage of over two orders of magnitude in power, and over an order of magnitude in area.

Fig. 18(a) shows the micrograph of the ASIC with reference electrodes and WEs shown. Fig. 18(b) depicts the $\Delta\Sigma$ ADC channel layout including comparator, DAC, counter, and pulse-shaping blocks. Fig. 19 depicts the system power breakdown.

VI. CONCLUSION

In this article, a 12-channel 0.13 μm CMOS impedance analyzer is presented. An antifouling layer on gold deposition technique is developed for selectively sensing potassium ions. The impedance analyzer employs an opamp-less first-order delta-sigma ($\Delta\Sigma$) ADC for current sensing. A compact multiplierless impedance analyzer VLSI architecture is presented. The current-sensing channel consumes 50 nW of power and

occupies 0.004 mm² of silicon area which are the lowest performance indicators for an integrated impedance analyzer. The SNDR is measured to be 50.3 dB with 1 pA sensitivity. The error in digital impedance calculation using the proposed 1-bit (square wave) MAC as compared with a 10-bit sine wave MAC is measured to be less than 2%. The design is validated by means of multisite potassium concentration measurements in the rodent brain.

ACKNOWLEDGMENT

The authors would like to thank CMC Microsystems for providing products and services that facilitated this article, including CAD tools for design and simulation, as well as integrated circuits fabrication services. Peter L. Carlen, Michael Thompson, and Roman Genov conceived, devised and oversaw this project and provided close direction for the entire team. Nima Soltani and Hossein Kassiri designed the impedance analyzer integrated circuit. Nima Soltani carried out the PCB design as well as prototyped and tested the electronic microsystem including the gold electrodes. Ruben Machado and Michael Thompson developed the antifouling layer chemistry on gold electrodes. Nima Soltani and Suzie Dufour tested the microsystem in optogenetic stimulation experiments in the rodent brain cortex. Maged ElAnsary contributed the mathematical analysis and the analytical model of the circuit. All authors conceived various elements of the experiments, analyzed the results and reviewed this article. Maged ElAnsary, Nima Soltani, Hossein Kassiri, and Roman Genov wrote and edited this article.

REFERENCES

- [1] M. E. Ladd *et al.*, “Pros and cons of ultra-high-field MRI/MRS for human application,” *Progr. Nucl. Magn. Reson. Spectrosc.*, vol. 109, pp. 1–50, Dec. 2018.
- [2] P. Padmawar, X. Yao, O. Bloch, G. T. Manley, and A. S. Verkman, “K+ waves in brain cortex visualized using a long-wavelength K+-sensing fluorescent indicator,” *Nature Methods*, vol. 2, no. 11, pp. 825–827, Nov. 2005.

- [3] K. Ohtsuka *et al.*, "Fluorescence imaging of potassium ions in living cells using a fluorescent probe based on a thrombin binding aptamer-peptide conjugate," *Chem. Commun.*, vol. 48, no. 39, p. 4740, 2012.
- [4] H. M. Jafari, K. Abdelhalim, L. Soleymani, E. H. Sargent, S. O. Kelley, and R. Genov, "Nanostructured CMOS wireless ultra-wideband label-free PCR-free DNA analysis SoC," *IEEE J. Solid-State Circuits*, vol. 49, no. 5, pp. 1223–1241, May 2014.
- [5] M. H. Nazari, H. Mazhab-Jafari, L. Leng, A. Guenther, and R. Genov, "CMOS neurotransmitter microarray: 96-channel integrated potentiostat with on-die microsensors," *IEEE Trans. Biomed. Circuits Syst.*, vol. 7, no. 3, pp. 338–348, Jun. 2013.
- [6] J. B. Wydallie *et al.*, "Spatiotemporal norepinephrine mapping using a high-density CMOS microelectrode array," *Lab Chip*, vol. 15, no. 20, pp. 4075–4082, 2015.
- [7] Y.-T. Liao, H. Yao, A. Lingley, B. Parviz, and B. P. Otis, "A 3- μ w CMOS glucose sensor for wireless contact-lens tear glucose monitoring," *IEEE J. Solid-State Circuits*, vol. 47, no. 1, pp. 335–344, Jan. 2012.
- [8] J. S. Park, T. Chi, J. Butts, T. Hookway, T. McDevitt, and H. Wang, "A multimodality CMOS sensor array for cell-based assay and drug screening," in *IEEE Int. Solid-State Circuits Conf. (ISSCC) Dig. Tech. Papers*, Feb. 2015, pp. 1–3.
- [9] H. Jafari, L. Soleymani, and R. Genov, "16-channel CMOS impedance spectroscopy DNA analyzer with dual-slope multiplying ADCs," *IEEE Trans. Biomed. Circuits Syst.*, vol. 6, no. 5, pp. 468–478, Oct. 2012.
- [10] C. Baj-Rossi *et al.*, "Full fabrication and packaging of an implantable multi-panel device for monitoring of metabolites in small animals," *IEEE Trans. Biomed. Circuits Syst.*, vol. 8, no. 5, pp. 636–647, Oct. 2014.
- [11] Y. Eminaga, M. Brischwein, J. Wiest, J. Clauss, S. Becker, and B. Wolf, "Self calibration of a planar dissolved oxygen sensor," *Sens. Actuators B, Chem.*, vol. 177, pp. 785–791, Feb. 2013.
- [12] F. Heer, M. Keller, G. Yu, J. Janata, M. Josowicz, and A. Hierlemann, "CMOS electro-chemical DNA-detection array with on-chip ADC," in *IEEE Int. Solid-State Circuits Conf. (ISSCC) Dig. Tech. Papers*, Feb. 2008, pp. 168–604.
- [13] M. El Ansary *et al.*, "50nW 5kHz-BW opamp-less $\Delta\Sigma$ impedance analyzer for brain neurochemistry monitoring," in *IEEE Int. Solid-State Circuits Conf. (ISSCC) Dig. Tech. Papers*, Feb. 2018, pp. 288–290.
- [14] R. Machado *et al.*, "Biofouling-resistant impedimetric sensor for array high-resolution extracellular potassium monitoring in the brain," *Biosensors*, vol. 6, no. 4, p. 53, 2016.
- [15] C. Yang, S. R. Jadhav, R. M. Worden, and A. J. Mason, "Compact low-power impedance-to-digital converter for sensor array microsystems," *IEEE J. Solid-State Circuits*, vol. 44, no. 10, pp. 2844–2855, Oct. 2009.
- [16] B. Goldstein, D. Kim, J. Xu, T. K. Vanderlick, and E. Culurciello, "CMOS low current measurement system for biomedical applications," *IEEE Trans. Biomed. Circuits Syst.*, vol. 6, no. 2, pp. 111–119, Apr. 2012.
- [17] M. Tohidian, I. Madadi, and R. B. Staszewski, "Analysis and design of a high-order discrete-time passive IIR low-pass filter," *IEEE J. Solid-State Circuits*, vol. 49, no. 11, pp. 2575–2587, Nov. 2014.
- [18] S. Pavan, R. Schreier, and G. C. Temes, *Understanding Delta-Sigma Data Converters*. Hoboken, NJ, USA: Wiley, 2017.
- [19] M. Stanacevic, K. Murari, A. Rege, G. Cauwenberghs, and N. V. Thakor, "VLSI potentiostat array with oversampling gain modulation for wide-range neurotransmitter sensing," *IEEE Trans. Biomed. Circuits Syst.*, vol. 1, no. 1, pp. 63–72, Mar. 2007.
- [20] J. L. A. de Melo, J. Goes, and N. Paulino, "0.7 V 256 μ W $\Delta\Sigma$ modulator with passive RC integrators achieving 76 dB DR in 2 MHz BW," in *Proc. Symp. VLSI Circuits (VLSI Circuits)*, Jun. 2015, pp. C290–C291.
- [21] B. Bozorgzadeh, D. R. Schuweiler, M. J. Bobak, P. A. Garris, and P. Mohseni, "Neurochemostat: A neural interface SoC with integrated chemometrics for closed-loop regulation of brain dopamine," *IEEE Trans. Biomed. Circuits Syst.*, vol. 10, no. 3, pp. 654–667, Jun. 2016.
- [22] B. Nowacki, N. Paulino, and J. Goes, "A 1 V 77 dB-DR 72 dB-SNDR 10 MHz-BW 2-1 MASH CT $\Delta\Sigma$ M," in *IEEE Int. Solid-State Circuits Conf. (ISSCC) Dig. Tech. Papers*, Jan. 2016, pp. 274–275.
- [23] A. F. Yeknami *et al.*, "A 0.3 V biofuel-cell-powered glucose/lactate biosensing system employing a 180 nW 64 dB SNR passive $\Delta\Sigma$ ADC and a 920 MHz wireless transmitter," in *IEEE Int. Solid-State Circuits Conf. (ISSCC) Dig. Tech. Papers*, Feb. 2018, pp. 284–286.



Maged ElAnsary (Member, IEEE) received the B.Sc. degree (Hons.) and the M.A.Sc. degree in electrical engineering from Ain Shams University, Cairo, Egypt, in 2010 and 2015, respectively, and the Ph.D. degree from the University of Toronto, Toronto, ON, Canada, in 2019.

From 2010 to 2015, he was a Senior Analog/Mixed-Signal Design Engineer with Si-Ware Systems (SWS), Cairo, designing high performance analog front ends and sensor interfaces. He is currently an Assistant Lecturer with Electronics and Communication Engineering Department, Ain Shams University. His research interests include ultralow power design of implantable, fully wireless SoCs for interfacing with the nervous system to be applied in biomedical applications for neurological disorders.

Dr. ElAnsary was a recipient of the Analog Devices Outstanding Student Designer Award in 2018. He has also served as a Reviewer for scientific journals including the IEEE TRANSACTIONS ON BIOMEDICAL CIRCUITS AND SYSTEMS and the IEEE SOLID-STATE CIRCUITS LETTERS (SSC-L).



Nima Soltani (Member, IEEE) received the B.Eng. and M.A.Sc. degrees in electrical engineering from Ryerson University, Toronto, ON, Canada, in 2007 and 2010, respectively, and the Ph.D. degree from the University of Toronto, Toronto, in 2016. His M.A.Sc. thesis focused on ultralow-power RF circuits for passive Microsystems, and RF power transmission. His doctoral dissertation focuses on inductively-powered implantable brain chemistry monitoring systems.

From 2010 to 2011, he was with Solace Power Inc., Mount Pearl, NL, Canada, on the development of the first electrical induction system for medium-range wireless power transfer. He is a Co-founder of BrainCom Inc., Toronto, a Toronto-based company specializing in the development of wearable and implantable platforms for high-resolution brain signal processing and acquisition.



Hossein Kassiri (Member, IEEE) received the B.Sc. degree from the University of Tehran, Tehran, Iran, and the M.A.Sc. degree from McMaster University, Hamilton, ON, Canada, and the Ph.D. degree from the University of Toronto, Toronto, ON, Canada, all in electrical and computer engineering, in 2008, 2010, and 2015, respectively.

He is currently an Assistant Professor with the Department of Electrical Engineering and Computer Science, York University, Toronto, where he is the Director of the Integrated Circuits and Systems Lab (ICSL) and Center for Microelectronics Prototyping and Test (MPT). His research interests lie primarily in the area of design and development of wireless and battery-less multimodal neural interfacing systems and their application in monitoring and treatment of neurological disorders.

Dr. Kassiri holds the position of CTO at BrainCom Inc., Toronto, a company he co-founded in September 2015, specialized in implantable brain-computer interfaces. He was a recipient of the IEEE ISSCC 2017 Jack Kilby Award for Outstanding Student Paper, the IEEE ISCAS Best Paper Award (BioCAS track) in 2016, the Ontario Brain Institute (OBI) Entrepreneurship Award in 2015, the Heffernan Commercialization Award in 2014, and the CMC Brian L. Barge Award for Excellence in Microsystems Integration in 2012. He has been an Associate Editor of the IEEE TRANSACTION ON BIOMEDICAL CIRCUITS AND SYSTEMS (TBioCAS) since January 2019.



Ruben Machado received the B.Sc. degree (Hons.) from the University of Toronto, Toronto, ON, Canada, in 2014, and the M.A.Sc. degree from the University of Aberdeen, Aberdeen, U.K., in 2016.

He is currently a Country Study Specialist with Roche, USA. He coordinates the operational aspects for the implementation of clinical trial activities from study startup through database lock, ensuring quality and safety standards, regulations, timelines, and budget commitments are met.



Michael Thompson (Senior Member, IEEE) is currently a Professor of bioanalytical chemistry with the University of Toronto, Toronto, ON, Canada. He has held a number of distinguished research posts including the Leverhulme Fellowship with the University of Durham, Durham, U.K., and the Science Foundation Ireland E.T.S Walton Research Fellowship with Tyndall National Institute, Cork City. He is recognized internationally for his pioneering work over many years in the area of research into new biosensor technologies and the surface chemistry of biochemical and biological entities. He has made major contributions to the label-free detection of immunochemical and nucleic acid interactions and surface behavior of cells using ultrahigh frequency acoustic wave physics.

Prof. Thompson has served on the Editorial Boards of a number of major international journals including *Analytical Chemistry and The Analyst*. He is currently the Editor-in-Chief of the monograph series Detection Science for the Royal Society of Chemistry, U.K. and an Associate Editor of the IEEE SENSORS.



Suzie Dufour received the B.Sc. degree in physics and the M.S. and Ph.D. degrees in neurobiology from Laval University, Quebec City, QC, Canada, in 2003, 2006, and 2012, respectively.

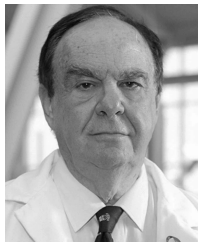
She is currently a Solution Manager with National Optics Institute (INO), Quebec City.



Roman Genov (Senior Member, IEEE) received the B.S. degree in electrical engineering from the Rochester Institute of Technology, Rochester, NY, USA, in 1996, and the M.S.E. and Ph.D. degrees in electrical and computer engineering from Johns Hopkins University, Baltimore, MD, USA, in 1998 and 2003, respectively.

He is currently a Professor with the Department of Electrical and Computer Engineering, University of Toronto, Toronto, ON, Canada, where he is a member of Electronics Group and Biomedical Engineering Group and the Director of Intelligent Sensory Microsystems Laboratory. His research interests are primarily in analog integrated circuits and systems for energy-constrained biological, medical, and consumer sensory applications.

Dr. Genov was a member of the IEEE International Solid-State Circuits Conference International Program Committee. He is also a member of the European Solid-State Circuits Conference International Program Committee. He was a co-recipient of the Jack Kilby Award for Outstanding Student Paper at IEEE International Solid-State Circuits Conference, the NSERC Discovery Accelerator Award, the Best Paper Award by the IEEE TRANSACTIONS ON BIOMEDICAL CIRCUITS AND SYSTEMS, the Best Paper Award at IEEE Biomedical Circuits and Systems Conference, the Best Paper Award in Biomedical Systems and Best Student Paper Award at IEEE International Symposium on Circuits and Systems, the Brian L. Barge Award for Excellence in Microsystems Integration, the MEMSCAP Microsystems Design Award, the DALSA Corporation Award for Excellence in Microsystems Innovation, and the Canadian Institutes of Health Research Next Generation Award. He was a Technical Program Co-Chair at the IEEE Biomedical Circuits and Systems Conference. He was an Associate Editor of the IEEE TRANSACTIONS ON CIRCUITS AND SYSTEMS-II: EXPRESS BRIEFS and the IEEE SIGNAL PROCESSING LETTERS. He is an Associate Editor of the IEEE TRANSACTIONS ON BIOMEDICAL CIRCUITS AND SYSTEMS, and its Guest Editor of Special Issues on the IEEE International Solid-State Circuits Conference.



Peter L. Carlen is currently a Professor in medicine (neurology) and physiology with the Institute of Biomaterials and Biomedical Engineering, University of Toronto, Toronto, ON, Canada.

He was formerly the Head of neurology with Addiction Research Foundation, Toronto. In 1989, he was appointed Director of the Playfair Neuroscience Unit and Neuroscience Research, University Health Network, for a 10-year term, where he is currently a Senior Scientist. He is an Active Neurological Clinician with University Health Network,

Toronto (Toronto Western Hospital) with a practice focused mainly on patients with epilepsy. He has over 300 peer-reviewed biomedical publications. He holds six patents. His main research interests are mechanisms, pharmacology, and control of neural synchrony and entrainment in epilepsy, sudden unexpected death in epilepsy (SUDEP), brain state classification, gap junctional communication, and using human cerebral organoids to study epilepsy.